Engineering and Technology
2015; 2(5): 297-311
Published online July 10, 2015 (http://www.aascit.org/journal/et)

American Association for Science and Technology

Keywords
Zhou *et al.* Model,
Kergaravat and Knight Model,
Yoder *et al.* Model,
Coakley Model,
Rumsey *et al.* Model,
Navier-Stokes Equations

Received: June 7, 2015
Revised: June 17, 2015
Accepted: June 18, 2015

Assessment of Several Turbulence Models as Applied to Supersonic Flows in 2D – Part IV

Edisson S. G. Maciel

Aeronautical Engineering Division (IEA), Aeronautical Technological Institute (ITA), São José dos Campos, SP, Brazil

Email address
edisavio@edissonsavio.eng.br

Citation
Edisson S. G. Maciel. Assessment of Several Turbulence Models as Applied to Supersonic Flows in 2D – Part IV. *Engineering and Technology.* Vol. 2, No. 5, 2015, pp. 297-311.

Abstract
In the present work, the Van Leer flux vector splitting scheme is implemented to solve the two-dimensional Favre-averaged Navier-Stokes equations. The Zhou, Davidson and Olsson, Kergaravat and Knight, Yoder, Georgiadids and Orkwis, Coakley, and Rumsey, Gatski, Ying and Bertelrud two-equation models are used in order to close the problem. The physical problem under study is the supersonic flow around a simplified version of the VLS (Brazilian “Satellite Launcher Vehice”) configuration. The results have demonstrated that the stagnation pressure ahead of the VLS configuration is better predicted by the Kergaravat and Knight turbulence model in its Launder and Spalding variant.

1. Introduction

Conventional non-upwind algorithms have been used extensively to solve a wide variety of problems ([1]). Conventional algorithms are somewhat unreliable in the sense that for every different problem (and sometimes, every different case in the same class of problems) artificial dissipation terms must be specially tuned and judicially chosen for convergence. Also, complex problems with shocks and steep compression and expansion gradients may defy solution altogether.

Upwind schemes are in general more robust but are also more involved in their derivation and application. Some upwind schemes that have been applied to the Euler equations are: [2-3]. Some comments about these methods are reported in [4]. The interested reader is encouraged to read this reference to become aware of the present study.

In relation to turbulent flow simulations, [5] applied the Navier-Stokes equations to transonic flows problems along a convergent-divergent nozzle and around the NACA 0012 airfoil. The [6] model was used to close the problem. Three algorithms were implemented: the [7] explicit scheme, the [8] implicit scheme and the [9] explicit scheme. The results have shown that, in general terms, the [7] and the [9] schemes have presented better solutions.

[10] have performed a study involving three different turbulence models. In this paper, the Navier-Stokes equations were solved applied to the supersonic flow around a simplified configuration of the Brazilian Satellite Launcher, VLS. The algebraic models of [11] and of [6] and the one-equation model of [12] were used to close the problem. The algorithms of [13] and of [3] were compared and presented good results.

In terms of two-equation models, [14] have presented a work that deals with such models applied to the solution of supersonic aerospace flow problems. The two-dimensional Navier-Stokes equations written in conservative form, employing a finite volume formulation and a structured spatial discretization were solved. The [2] algorithm, first order accurate in space, was used to perform the numerical experiments. Turbulence was taken into account using two k-ε turbulence models, namely: the [15-16] models. The steady state supersonic flow around a simplified version of the Brazilian Satellite Launcher, VLS, configuration was studied. The results have shown that the pressure field generated by the [16] model was stronger than the respective one obtained with the [15] model, although the latter predicts more accurate aerodynamic coefficients in this problem. The [16] model predicted less intense turbulence kinetic energy- and dissipation-rate profiles than the [15] model, yielding less intense turbulence fields.

In the present work, the [2] flux vector splitting scheme is implemented, on a finite-volume context. The two-dimensional Favre-averaged Navier-Stokes equations are solved using an upwind discretization on a structured mesh. The [16-20] two-equation models are used in order to close the problem. The physical problem under study is the supersonic flow around a simplified version of the VLS configuration. The implemented scheme uses a MUSCL procedure to reach second order accuracy in space. The time integration uses a Runge-Kutta method of five stages and is second order accurate. The algorithm is accelerated to the steady state solution using a spatially variable time step. This technique has proved excellent gains as reported in [21-22].

The results have demonstrated that the [16] model in its Launder and Spalding variant has yielded more critical pressure field than the others models. The aerodynamic coefficient of lift is better predicted by the [16] turbulence model in its Launder and Spalding variant. Finally, the stagnation pressure ahead of the VLS configuration is better predicted by the [16] turbulence model in its Launder and Spalding variant. Hence, the best choice corresponds to the [16] turbulence model in its LS variant for this study.

2. Navier-Stokes Equations

The two-dimensional flow is modeled by the Navier-Stokes equations, which express the conservation of mass and energy as well as the momentum variation of a viscous, heat conducting and compressible media, in the absence of external forces. The Navier-Stokes equations are presented in their two-equation turbulence model formulation. The integral form of these equations may be represented by:

$$\partial/\partial t\int_V Q dV + \int_S\left[\left(E_e - E_v\right)n_x + \left(F_e - F_v\right)n_y\right]dS + \int_V G dV = 0, \qquad (1)$$

where Q is written for a Cartesian system, V is the cell volume, n_x and n_y are components of the unity vector normal to the cell boundary, S is the flux area, E_e and F_e are the components of the convective, or Euler, flux vector, E_v and F_v are the components of the viscous, or diffusive, flux vector and G is the source term of the two-equation models. The vectors Q, E_e, F_e, E_v and F_v are, incorporating a k-ε or k-ω formulation, represented by:

$$Q = \begin{Bmatrix} \rho \\ \rho u \\ \rho v \\ e \\ \rho k \\ \rho s \end{Bmatrix},\ E_e = \begin{Bmatrix} \rho u \\ \rho u^2 + p \\ \rho uv \\ (e+p)u \\ \rho ku \\ \rho su \end{Bmatrix},\ F_e = \begin{Bmatrix} \rho v \\ \rho uv \\ \rho v^2 + p \\ (e+p)v \\ \rho kv \\ \rho sv \end{Bmatrix},\ E_v = \begin{Bmatrix} 0 \\ t_{xx}+\tau_{xx} \\ t_{xy}+\tau_{xy} \\ f_x \\ \alpha_x \\ \beta_x \end{Bmatrix};F_v = \begin{Bmatrix} 0 \\ t_{xy}+\tau_{xy} \\ t_{yy}+\tau_{yy} \\ f_y \\ \alpha_y \\ \beta_y \end{Bmatrix},\ \text{and } G = \begin{Bmatrix} 0 \\ 0 \\ 0 \\ 0 \\ G_k \\ G_s \end{Bmatrix}, \qquad (2)$$

where the components of the viscous stress tensor are defined as:

$$\begin{aligned} t_{xx} &= \left[2\mu_M \partial u/\partial x - 2/3\mu_M\left(\partial u/\partial x + \partial v/\partial y\right)\right]/Re; \\ t_{xy} &= \mu_M\left(\partial u/\partial y + \partial v/\partial x\right)/Re; \\ t_{yy} &= \left[2\mu_M\left(\partial v/\partial y\right) - 2/3\mu_M\left(\partial u/\partial x + \partial v/\partial y\right)\right]/Re. \end{aligned} \qquad (3)$$

The components of the turbulent stress tensor (Reynolds stress tensor) are described by the following expressions:

$$\begin{aligned} \tau_{xx} &= \left[2\mu_T \partial u/\partial x - 2/3\mu_T\left(\partial u/\partial x + \partial v/\partial y\right)\right]/Re - 2/3\rho k; \\ \tau_{xy} &= \mu_T\left(\partial u/\partial y + \partial v/\partial x\right)/Re; \\ \tau_{yy} &= \left[2\mu_T \partial v/\partial y - 2/3\mu_T\left(\partial u/\partial x + \partial v/\partial y\right)\right]/Re - 2/3\rho k. \end{aligned} \qquad (4)$$

Expressions to f_x and f_y are given below:

$$f_x = \left(t_{xx}+\tau_{xx}\right)u + \left(t_{xy}+\tau_{xy}\right)v - q_x; \qquad (5)$$

$$f_y = \left(t_{xy}+\tau_{xy}\right)u + \left(t_{yy}+\tau_{yy}\right)v - q_y, \qquad (6)$$

where q_x and q_y are the Fourier heat flux components and are given by:

$$q_x = -\gamma/Re\left(\mu_M/Pr_L + \mu_T/Pr_T\right)\partial e_i/\partial x; \qquad (7)$$

$$q_y = -\gamma/Re\left(\mu_M/Pr_L + \mu_T/Pr_T\right)\partial e_i/\partial y. \qquad (8)$$

The diffusion terms related to the k-s equations are defined as:

$$\begin{aligned} \alpha_x &= 1/Re\left(\mu_M + \mu_T/\sigma_k\right)\partial k/\partial x; \\ \alpha_y &= 1/Re\left(\mu_M + \mu_T/\sigma_k\right)\partial k/\partial y; \end{aligned} \qquad (9)$$

$$\begin{aligned} \beta_x &= 1/Re\left(\mu_M + \mu_T/\sigma_s\right)\partial s/\partial x; \\ \beta_y &= 1/Re\left(\mu_M + \mu_T/\sigma_s\right)\partial s/\partial y. \end{aligned} \qquad (10)$$

In the above equations, ρ is the fluid density; u and v are Cartesian components of the velocity vector in the x and y directions, respectively; e is the total energy per unit volume; p is the static pressure; k is the turbulence kinetic energy; s is the second turbulent variable, which is the rate of dissipation of the turbulence kinetic energy (k-ε model) or the flow vorticity (k-ω model); the t's are viscous stress components; τ's are the Reynolds stress components; the q's are the Fourier heat flux components; G_k takes into account the production and the dissipation terms of k; G_s takes into account the production and the dissipation terms of s; μ_M and μ_T are the molecular and the turbulent viscosities, respectively; Pr_L and Pr_T are the laminar and the turbulent Prandtl numbers, respectively; σ_k and σ_s are turbulence coefficients; γ is the ratio of specific heats; Re is the laminar Reynolds number, defined by:

$$Re = \rho V_{REF} l_{REF} / \mu_M \,, \tag{11}$$

where V_{REF} is a characteristic flow velocity and l_{REF} is a configuration characteristic length. The internal energy of the fluid, e_i, is defined as:

$$e_i = e/\rho - 0.5\left(u^2 + v^2\right). \tag{12}$$

The molecular viscosity is estimated by the empirical Sutherland formula:

$$\mu_M = bT^{1/2} / (1 + S/T), \tag{13}$$

where T is the absolute temperature (K), b = 1.458×10^{-6} $Kg/(m.s.K^{1/2})$ and S = 110.4 K, to the atmospheric air in the standard atmospheric conditions ([23]).

The Navier-Stokes equations are dimensionless in relation to the freestream density, ρ_∞, the freestream speed of sound, a_∞, and the freestream molecular viscosity, μ_∞. The system is closed by the state equation for a perfect gas:

$$p = (\gamma - 1)\left[e - 0.5\rho\left(u^2 + v^2\right) - \rho k\right], \tag{14}$$

considering the ideal gas hypothesis. The total enthalpy is given by $H = (e + p)/\rho$.

The numerical algorithm is described in [4] and the interested reader is encouraged to read this reference to become familiar with the solver. Moreover, the MUSCL approach used to obtain TVD properties and high resolution is also described in [4] and the interested reader is invocated to read this reference. The spatially variable time step is detailed in [4] and is also recommended to read.

3. Turbulence Models

3.1. Zhou, Davidson, and Olsson Turbulence Model

To the [17] turbulence model, s = ε. Before defining the turbulent viscosity, it is necessary to define some parameters. The coefficient C_l is defined as

$$C_l = \kappa C_\mu^{-0.75}. \tag{15}$$

The characteristic viscous length is expressed as

$$l_\mu = C_l N\left[1 - e^{-\sqrt{k}N/(A_\mu \nu_m)}\right], \tag{16}$$

where N is the normal distance of a cell from the wall. The turbulent viscosity is defined as

$$\mu_T = Re\, C_\mu \rho \sqrt{k}\, l_\mu. \tag{17}$$

The characteristic temperature length is expressed as

$$l_t = C_3 N\left[1 - e^{-\sqrt{k}N/(C_4 \nu_m)}\right]. \tag{18}$$

The variable turbulent Prandtl number, to be inserted in Eqs. (7-8), is defined as

$$Pr_{T,var} = l_\mu / l_t. \tag{19}$$

The G_k and G_ε terms have the following expressions:

$$G_k = -P_k + D_k \quad \text{and} \quad G_\varepsilon = -P_\varepsilon + D_\varepsilon, \tag{20}$$

where:

$$\tau_{xy} = \mu_T\left(\frac{\partial u}{\partial y} + \frac{\partial v}{\partial x}\right)\Big/ Re,\ P_k = \tau_{xy}\frac{\partial u}{\partial y};\ D_k = \rho\varepsilon/Re; \tag{21}$$

$$P_\varepsilon = \frac{\varepsilon}{k} C_{1\varepsilon} P_k,\ D_\varepsilon = \frac{\varepsilon}{k} C_{2\varepsilon}\, \rho\varepsilon/Re. \tag{22}$$

The closure coefficients assume the following values: $C_{1\varepsilon} = 1.44$, $C_{2\varepsilon} = 1.92$, $C_3 = 3.12$, $C_4 = 92.0$, $\kappa = 0.40$, $A_\mu = 70.0$, $C_\mu = 0.09$, $\sigma_k = 1.0$, $\sigma_\varepsilon = 1.3$ and $Pr_L = 0.72$.

3.2. Kergaravat and Knight Turbulence Model

To the [16] turbulence model, s = ε_s. The [16] turbulence model presents two formulations to calculate the G_k and G_ε terms. The first related to [29] and the second due to [26]. In the [29] option, the turbulent viscosity is calculated from the turbulent Mach number:

$$M_t = \sqrt{2k/a^2}, \tag{23}$$

where "a" is the speed of sound. The dilatation dissipation is defined as

$$\varepsilon_d = C_k M_t^2 \varepsilon_s \tag{24}$$

and the total dissipation is

$$\varepsilon = \varepsilon_s + \varepsilon_d. \tag{25}$$

The turbulent viscosity is hence defined as

$$\mu_T = \mathrm{Re}\, C_\mu \rho\, k^2 / \varepsilon \,. \tag{26}$$

On the other hand, the turbulent viscosity calculated by [26] employs the dissipation rate equaled to the solenoid dissipation:

$$\varepsilon = \varepsilon_s \,. \tag{27}$$

The turbulent viscosity to this formulation is expressed as:

$$\mu_T = \mathrm{Re}\, C_\mu\, \rho k^2 / \varepsilon \left(1 - e^{-C_3 n^+}\right), \tag{28}$$

where:

$$n^+ = \mathrm{Re}\left(n\, u_* / \nu_w\right),\ u_* = \left(\tau_w/\rho_w\right)^{0,5} \text{ and } \nu_w = \left(\mu_M\right)_w / \rho_w \,, \tag{29}$$

with "n" being the normal distance from one cell to the wall, ν_w is the wall cinematic viscosity, τ_w is the wall tangential stress, ρ_w is the wall fluid density and $(\mu_M)_w$ is the wall molecular viscosity.

The G_k and G_ε terms have the following expressions:

$$G_k = -P_k + D_k \quad \text{and} \quad G_\varepsilon = -P_\varepsilon + D_\varepsilon \,, \tag{30}$$

where:

$$P_k = \tau_{xy}\, \partial u / \partial y; \quad D_k = \begin{cases} \rho\varepsilon, & [29] \\ \rho\varepsilon_s + 2\mu_M k / \left(n^2\, \mathrm{Re}\right), & [26] \end{cases}; \tag{31}$$

$$P_\varepsilon = C_{\varepsilon 1} P_k\, \varepsilon_s / k; \quad D_\varepsilon = \begin{cases} C_{\varepsilon 2} \rho \varepsilon_s^2 / k, & [29] \\ C_{\varepsilon 2} f_2 \rho \varepsilon_s^2 / k + 1/\mathrm{Re}\left(2\mu_M \varepsilon_s / n^2\right) e^{-C_4 n^+}, & [26] \end{cases}, \tag{32}$$

with:

$$f_2 = 1 - \left(0.4/1.8\right) e^{-\left(\mathrm{Re}\, k^2/(6\nu\varepsilon_s)\right)^2} \quad \text{and} \quad \nu = \mu_M / \rho \,. \tag{33}$$

The closure coefficients have their values given in Tab. 1. The laminar and turbulent Prandtl numbers have the following values: $Pr_L = 0.72$ and $Pr_T = 0.9$.

Table 1. *Closure coefficients ([16] model).*

Constant	[29]	[26]
σ_k	1.0	1.0
σ_ε	1.3	1.3
C_μ	0.09	0.09
$C_{\varepsilon 1}$	1.44	1.35
$C_{\varepsilon 2}$	1.92	1.80
C_3	-	0.0115
C_4	-	0.5
C_k	1.0	-

3.3. Yoder, Georgiadids, and Orkwis Turbulence Model

To the [18] model, s = ω. The turbulent Reynolds number is specified by:

$$\mathrm{Re}_T = \rho k / \left(\mu_M \omega\right). \tag{34}$$

The parameter α^* is given by:

$$\alpha^* = \left(\alpha_0^* + \mathrm{Re}_T / R_k\right) / \left(1 + \mathrm{Re}_T / R_k\right). \tag{35}$$

The turbulent viscosity is specified by:

$$\mu_T = \mathrm{Re}\, \alpha^* \rho k / \omega \,. \tag{36}$$

The source term denoted by G in the governing equations contains the production and dissipation terms of k and ω. To the [18] model, the G_k and G_ω terms have the following expressions:

$$G_k = -P_k + D_k \quad \text{and} \quad G_\omega = -P_\omega + D_\omega \,. \tag{37}$$

To define the production and dissipation terms, it is necessary to define firstly some parameters. The turbulent Mach number is defined as:

$$M_T = \sqrt{2k / a^2} \,. \tag{38}$$

It is also necessary to specify the function F:

$$F = \mathrm{MAX}\left(M_T^2 - M_{T,0}^2,\, 0.0\right). \tag{39}$$

The β^* parameter is given by:

$$\beta^* = 0.09\left[5/18 + \left(\mathrm{Re}_T / R_S\right)^4\right] / \left[1 + \left(\mathrm{Re}_T / R_S\right)^4\right] \tag{40}$$

Finally, the production and dissipation terms of Eq. (37) are given by

$$P_k = \mu_T \left(\frac{\partial u}{\partial y} + \frac{\partial v}{\partial x}\right) \frac{\partial u}{\partial y}; \; D_k = \beta^* \rho \omega k \left(1 + \xi_k F\right) / \mathrm{Re}; \tag{41}$$

$$P_\omega = \alpha\omega / k P_k \,; \text{ and } D_\omega = \rho\omega^2 \left(\beta + \beta^* \xi_\omega F\right) / \mathrm{Re} \,, \tag{42}$$

with:

$$\alpha = 5/9\left(\alpha_0 + \mathrm{Re}_T / R_\omega\right)\left(1 + \mathrm{Re}_T / R_\omega\right) / \alpha^* \,. \tag{43}$$

The [18] turbulence model adopts the following closure coefficients: $R_s = 8.0$, $R_k = 6.0$, $R_\omega = 2.7$, $\xi_k = 1.0$, $\xi_\omega = 0.0$, $\beta = 3/40$, $M_{T,0} = 0.0$, $\alpha_0 = 0.1$, $\alpha_0^* = \beta/3$, $\sigma_k = 2.0$ and $\sigma_\omega = 2.0$.

3.4. Coakley Turbulence Model

In the [19] turbulence model, s = ω. The turbulent viscosity is expressed in terms of k and ω as:

$$\mu_T = \mathrm{Re}\, C_\mu \rho k / \omega . \tag{44}$$

In this model, the quantities σ_k and σ_ω have the values $1/\sigma^*$ and $1/\sigma$, respectively, where σ^* and σ are model constants.

The source term denoted by G in the governing equations contains the production and dissipation terms of k and ω. To the [19] model, the G_k and G_ω terms have the following expressions:

$$G_k = -P_k - D_k \quad \text{and} \quad G_\omega = -P_\omega - D_\omega . \tag{45}$$

To define the production and dissipation terms, it is necessary to define firstly some parameters. The $S_{i,j}$ gradient is defined as

$$S_{ij} = 0.5\left(\frac{\partial u}{\partial y} + \frac{\partial v}{\partial x}\right). \tag{46}$$

The gradient S is expressed as

$$S = \sqrt{2 S_{ij} S_{ij}} . \tag{47}$$

The η parameter is defined as

$$\eta = S/\omega . \tag{48}$$

The divergent and the parameter λ are determined by

$$D = \frac{\partial u}{\partial x} + \frac{\partial v}{\partial y} \quad \text{and} \quad \lambda = \frac{D}{\omega} . \tag{49}$$

The coefficient α_k and α_ω are defined by

$$\alpha_k = \frac{2}{3}\left(1 + C_\mu \lambda\right) \quad \text{and} \quad \alpha_\omega = \alpha_k . \tag{50}$$

The terms of production and destruction of kinetic energy are defined as

$$P_k = C_\mu \eta^2 \rho\omega k/\mathrm{Re} \quad \text{and} \quad D_k = -\left(\alpha_k \lambda + 1\right)\rho\omega k/\mathrm{Re} . \tag{51}$$

In relation to the terms of production and destruction of vorticity, new terms are defined. The characteristic turbulent length is expressed as

$$l = \sqrt{k}/\omega . \tag{52}$$

The coefficients $\theta_{k\omega}$ and θ_ω are defined as

$$\theta_{k\omega} = l^2 \frac{\partial k}{\partial y}\frac{\partial \omega}{\partial y}\Big/(k\omega) \quad \text{and} \quad \theta_\omega = l^2 \left(\frac{\partial \omega}{\partial y}\right)^2 \Big/ \omega^2 . \tag{53}$$

The turbulent Reynolds number is determined by

$$R_t = \frac{k}{\nu_m \omega} . \tag{54}$$

Some others parameters are defined

$$R = C_\mu R_t / R_o ,\ D_v = \mathrm{TANH}(R), \theta = \frac{\theta_{k\omega} - \theta_\omega}{D_v} ; \tag{55}$$

$$\Delta\theta = \mathrm{TANH}\left(|\theta| - \theta\right),\ f_{ii} = \frac{dp/dx}{\rho\sqrt{k\omega}},\ f_i = f_{ii}^2 ; \tag{56}$$

$$\Delta f_i = \mathrm{TANH}\left(\alpha f_i\right),\ \Delta w = 1 - \Delta\theta\left(1 - D_v^4\right); \tag{57}$$

$$C_1 = 0.675(1 - \Delta w) + (0.35 + 0.25\Delta f_i)\Delta w ; \tag{58}$$

$$\sigma_w = (C_2 - C_1)\sqrt{C_\mu}\Big/\kappa^2 ,\ dw = 2\sigma_w \Delta w C_\mu \theta_{k\omega} . \tag{59}$$

Finally, the production and destruction terms of vorticity are defined as

$$P_\omega = C_1 C_\mu \eta^2 \rho\omega^2/\mathrm{Re} \quad \text{and} \quad D_\omega = \left(-C_1\alpha_\omega\lambda - C_2 + dw\right)\rho\omega^2/\mathrm{Re}. \tag{60}$$

The closure coefficients assume the following values: $C_\mu = 0.09$, $C_2 = 0.833$, $\alpha = 5.0$, $\sigma_k = 1.0$, $\sigma = 0.5$, $\sigma^* = 0.5$, $\kappa = 0.41$, $R_o = 10.0$, $Pr_L = 0.72$ and $Pr_T = 0.9$.

3.5. Rumsey, Gatski, Ying, and Bertelrud Turbulence Model

Finally, the k-ω model of [20] is studied, where s = ω. The equilibrium eddy-viscosity term employed in the diffusion terms is given by

$$\mu_T^* = \mathrm{Re}\, c_\mu^* \rho k/\omega , \tag{61}$$

where $c_\mu^* = 0.081$.

The explicit nonlinear constitutive equation that is used to close the Reynolds-averaged Navier-Stokes equations is given (after regularization)

$$\rho\tau_{ij} = \frac{2}{3}\rho k \delta_{ij} - 2\mu_t\left(S_{ij} - \frac{1}{3}S_{kk}\delta_{ij}\right) - \frac{2\mu_t'\alpha_3}{\omega}\left(S_{ik}W_{kj} + S_{jk}W_{ki}\right) + \frac{4\mu_t'\alpha_2}{\omega}\left(S_{ik}S_{kj} - \frac{1}{3}S_{kl}S_{kl}\delta_{ij}\right), \tag{62}$$

where

$$S_{ij} = \frac{1}{2}\left(\frac{\partial u_i}{\partial x_j} + \frac{\partial u_j}{\partial x_i}\right) \quad \text{and} \quad W_{ij} = \frac{1}{2}\left(\frac{\partial u_i}{\partial x_j} - \frac{\partial u_j}{\partial x_i}\right) \quad (63)$$

are the mean-rate-of-strain tensor and the mean-vorticity tensor, respectively. The turbulent viscosity μ_T is

$$\mu_T = \mathrm{Re}\, c_\mu \rho k / \omega . \quad (64)$$

and

$$c_\mu = \frac{3(1+\eta^2) + 0.2(\eta^6 + \zeta^6)}{3 + \eta^2 + 6\eta^2\zeta^2 + 6\zeta^2 + \eta^6 + \zeta^6}\alpha_1 ; \quad (65)$$

$$\eta = (\alpha_2/\omega)(S_{ij}S_{ij})^{\frac{1}{2}} \quad \text{and} \quad \zeta = (\alpha_3/\omega)(W_{ij}W_{ij})^{\frac{1}{2}}, \quad (66)$$

where:

$$\alpha_1 = (4/3\text{-}C_2)(g/2);\ \alpha_2 = (2\text{-}C_3)(g/2);\ \alpha_3 = (2\text{-}C_4)(g/2); \quad (67)$$

$$g = (C_1/2+C_5\text{-}1)\text{-}1. \quad (68)$$

The constants that govern the pressure-strain correlation model of [27] are $C_1 = 6.8$, $C_2 = 0.36$, $C_3 = 1.25$, $C_4 = 0.4$ and $C_5 = 1.88$. The μ_T' terms are given by

$$\mu_T' = \mathrm{Re}\, c_\mu' \rho k / \omega , \quad (69)$$

where

$$c_\mu' = \frac{3(1+\eta^2)}{3 + \eta^2 + 6\eta^2\zeta^2 + 6\zeta^2 + \eta^6 + \zeta^6}\alpha_1 . \quad (70)$$

The source term denoted by G in the governing equation contains the production and dissipation terms of k and ω. To the [20] model, the G_k and G_ω terms have the following expressions:

$$G_k = -P_k + D_k \quad \text{and} \quad G_\omega = -P_\omega + D_\omega , \quad (71)$$

where:

$$P_k = \rho\mu_T\left(\frac{\partial u}{\partial y} + \frac{\partial v}{\partial x}\right)\frac{\partial u}{\partial y},\ D_k = \rho\omega k/\mathrm{Re}; \quad (72)$$

$$P_\omega = \psi\rho\omega/kP_k \ , \quad \text{and} \quad D_\omega = \beta\rho\omega^2/\mathrm{Re}. \quad (73)$$

The closure coefficients adopted to the [20] model assume the following values: $\beta = 0.83$; $\kappa = 0.41$; $\sigma_k = 1.4$; $\sigma_\omega = 2.2$; $Prd_L = 0.72$; $Prd_T = 0.9$; $\psi = \beta - \left[\kappa^2/\sigma_\omega\sqrt{c_\mu^*}\right]$.

4. Initial and Boundary Conditions

The initial and boundary conditions to the [16-20] turbulence models are detailed in [4; 24]. The interested reader is encouraged to read these references to become familiar with these procedures.

5. Results

Tests were performed in a Dual Core processor of 2.3GHz and 2.0Gbytes of RAM microcomputer. Three orders of reduction of the maximum residual in the field were considered to obtain a converged solution. The residual was defined as the value of the discretized conservation equation. The entrance or attack angle was adopted equal to zero. The ratio of specific heats, γ, assumed the value 1.4.

Figures 1 shows the entire VLS viscous mesh, whereas Fig. 2 shows the detail of the VLS close to the satellite compartment. A mesh of 253x70 points or composed of 17,388 rectangular cells and 17.710 nodes was generated, employing an exponential stretching of 5% in the η direction.

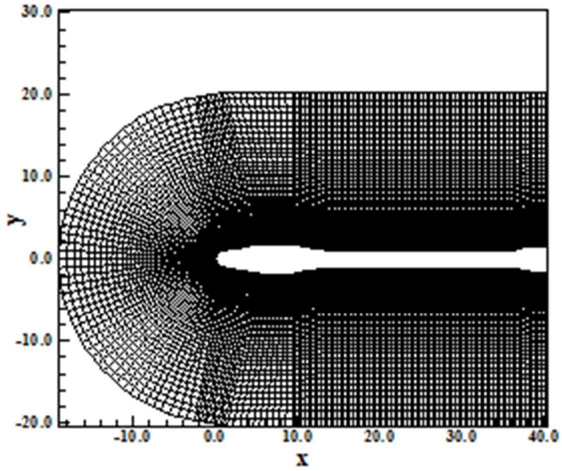

Figure 1. *VLS viscous mesh.*

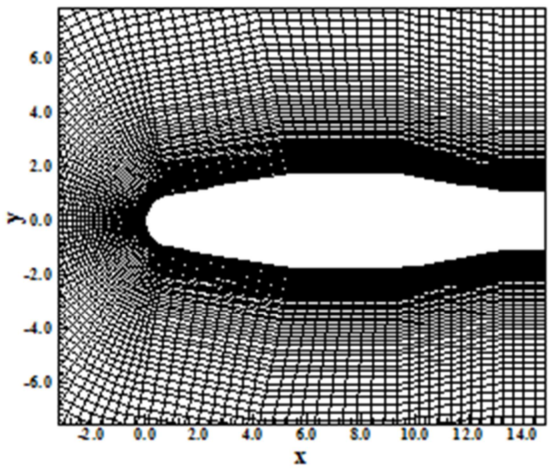

Figure 2. *Detail of the satellite compartment.*

The initial data of the simulations are described in Tab. 2.

Table 2. *Initial Conditions.*

M_∞	θ	Altitude	L_∞	Re
3.0	0.0°	40,000m	3.76m	8.93×10^5

5.1. Zhou, Davidson, and Olsson Results

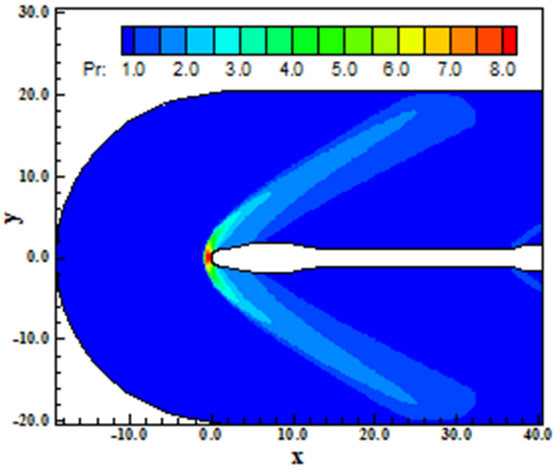

Figure 3. Pressure contours (ZDO).

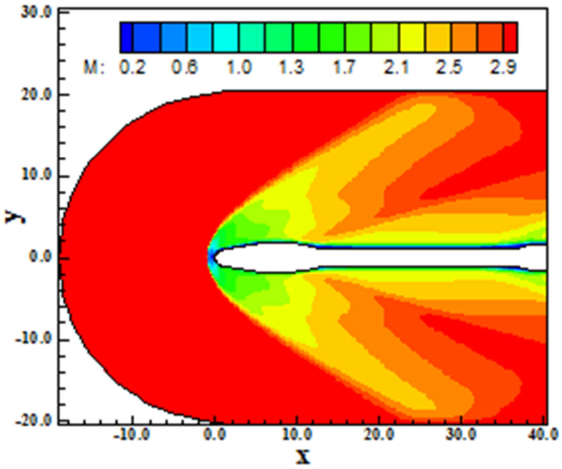

Figure 4. Mach number contours (ZDO).

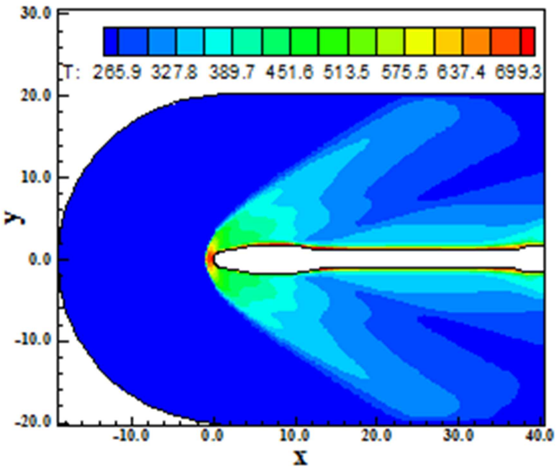

Figure 5. Temperature contours (ZDO).

Figure 3 exhibit the pressure contours obtained by the second order [2] scheme as using the [17] turbulence model. The contours are uniform and well defined. The normal shock wave at the blunt body nose is well captured. Figure 4 exhibits the Mach number contours obtained by the high resolution TVD [2] scheme. The viscous region close to the VLS walls is well captured; in other words, the heat conduction, through the Fourier law, is well captured by the turbulence model. The normal shock weave is well captured. The solution is free of pre-shock oscillations.

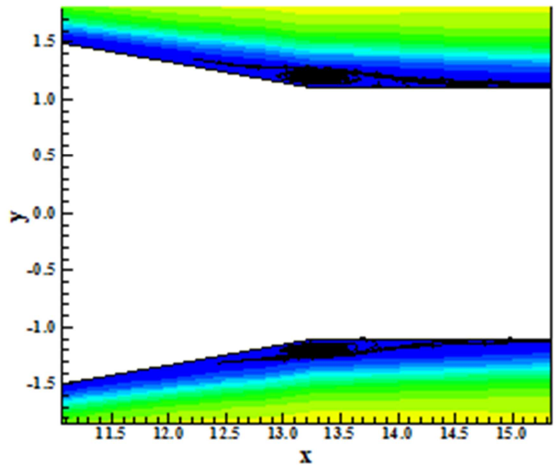

Figure 6. Circulation bubble formation (Cockpit-ZDO).

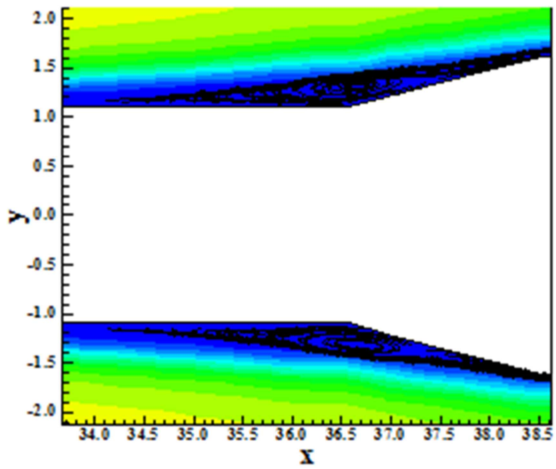

Figure 7. Circulation bubble formation (Boosters-ZDO).

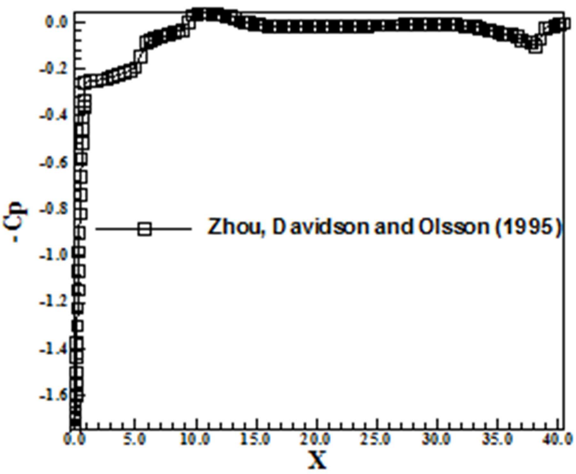

Figure 8. –Cp distribution (SA).

Figure 5 presents the translational/rotational temperature contours obtained by the [2] scheme. Temperatures around 699.3 K are obtained. The region downstream the satellite compartment appears with regions of discrete high dissipation, as can be noted in the figure. In other words, this means that circulation bubbles are formed as consequence of boundary layer detachment. This behavior is also observed at the booster region. These can be seen in Figs. 6 and 7, which highlight the circulation bubble formations downstream the satellite compartment and upstream the booster region.

These regions are very discrete, but even so the numerical scheme was able to capture such phenomenon.

Figure 8 shows the –Cp distribution along the blunt body wall. The –Cp suffers a rapid increase in steps at the satellite compartment and downstream it is horizontal. At the booster region, a rapid decrease in the –Cp values with a recovery pressure at the ramp is observed. In all this distribution, no overshoots and undershoots are perceptible, even for a second-order scheme. This aspect highlights the MUSCL procedure as a good tool to provide clean profiles. Such procedure avoids the appearance of Gibbs phenomenon, typical of second order schemes, yielding good quality solutions.

5.2. Kergaravat and Knight Results

Launder and Spalding Option. Figure 9 shows the pressure contours obtained by the [2] scheme as using the [16] turbulence model in its Launder and Spalding variant. The shock is well defined and homogeneous. As can be seen, there are qualitative differences between this plot and the [17] corresponding plot. The shock at the booster region is captured by both models, but in the [16] turbulence model it is more spread out.

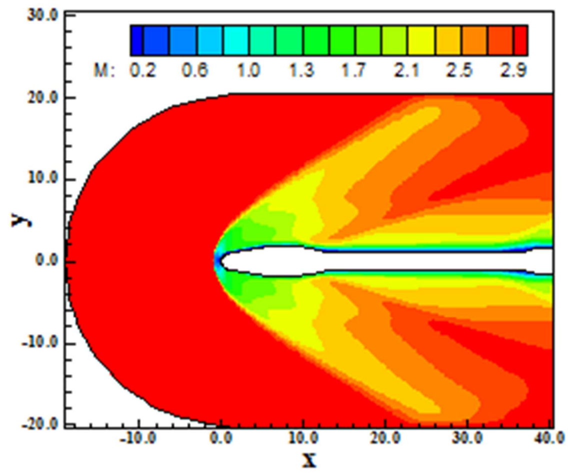

Figure 10. *Mach number contours (KK-LS).*

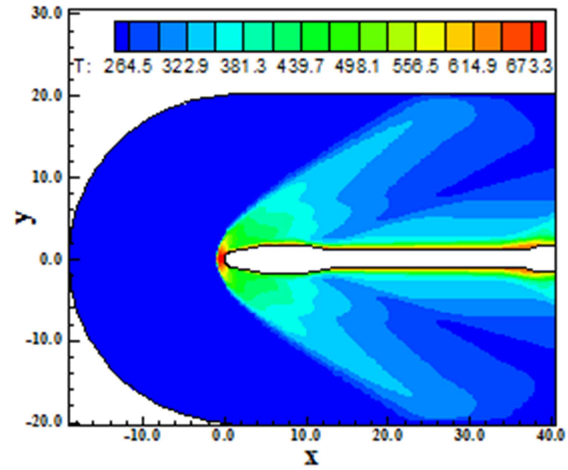

Figure 11. *Temperature contours (KK-LS).*

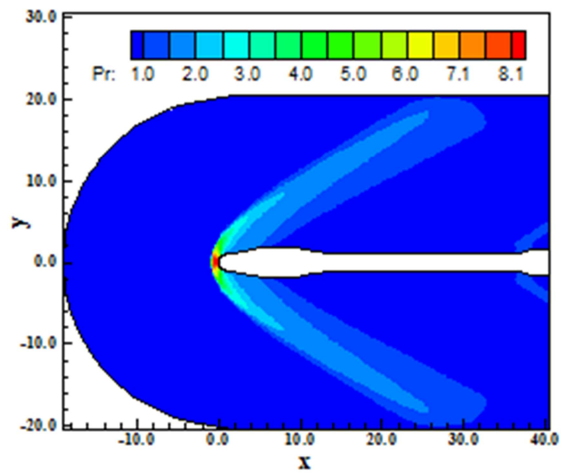

Figure 9. *Pressure contours (KK-LS).*

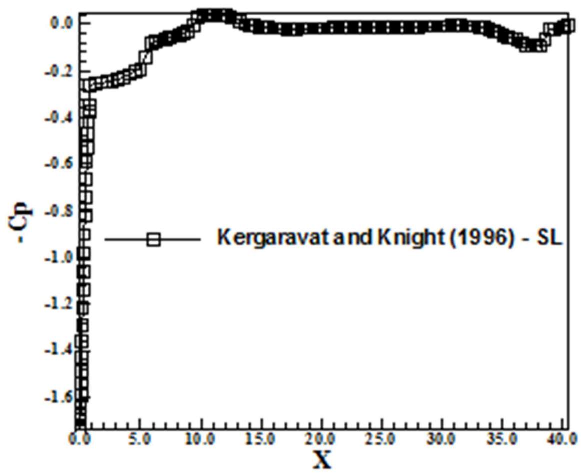

Figure 12. *–Cp distribution (KK-LS).*

Figure 10 exhibits the Mach number contours obtained by the [2] numerical scheme as using the [16] turbulence model. The present contours are similar to the corresponding [17] solution. The normal shock at the blunt nose is well captured by the scheme.

Figure 11 presents the temperature field obtained by the [2] scheme as using the [16] turbulence model. Qualitatively, this plot has differences in relation to the [17] plot. The [17] solution seems more dissipative. Moreover, the regions of high dissipation are concentrated at the satellite compartment end and at the booster region beginning. Temperatures close to 673.3 K are reached, less severe than the corresponding [17] temperature field.

Despite the good results, no regions of circulation bubbles are captured by the [16] turbulence model. The satellite compartment end and the booster region beginning are free of circulation bubble formation, which is a severe penalization to this turbulence model. This separation was captured by all turbulence models of this work and of [4; 24; 28], what becomes improbable its inexistence.

Figure 12 presents the –Cp distribution at wall of the VLS configuration, generated by the [16] turbulence model. This curve presents a reduction of –Cp close to the booster region and after that the pressure coefficient is recovered at the booster end. The –Cp distribution along the VLS central body is relative smooth, without oscillations in the solution.

Chien Option. Figure 13 shows the pressure contours obtained by the [2] scheme as using the [16] turbulence model in its Chien variant. The shock is well defined and homogeneous. As can be seen, there are qualitative differences between this plot and the [17] corresponding plot. The shock at the booster region is captured by both models, but in the [16] turbulence model it is more spread out.

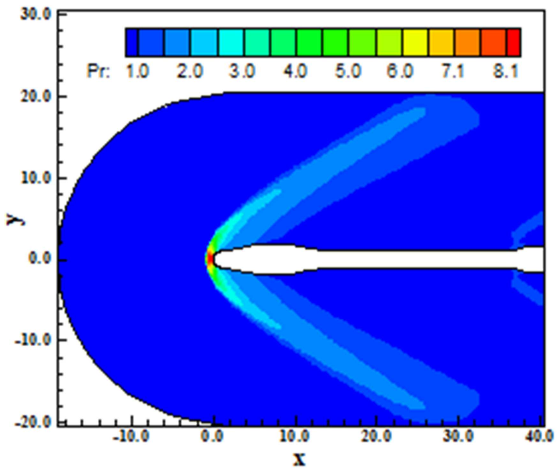

Figure 13. *Pressure contours (KK-C).*

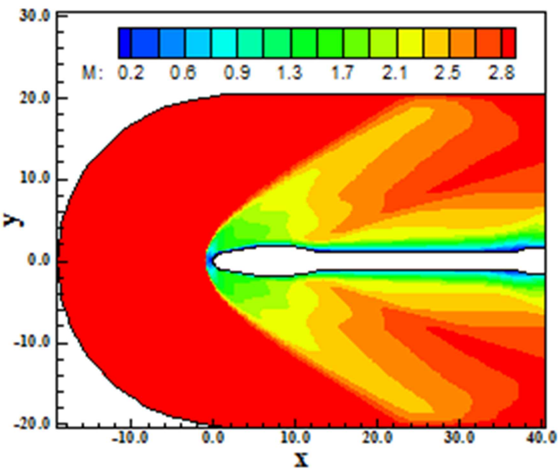

Figure 14. *Mach number contours (KK-C).*

Figure 14 exhibits the Mach number contours obtained by the [2] numerical scheme as using the [16] turbulence model. The present contours are similar to the corresponding [17] solution. The normal shock at the blunt nose is well captured by the scheme.

Figure 15 presents the temperature field obtained by the [2] scheme as using the [16] turbulence model. Qualitatively, this plot has differences in relation to the [17] plot. The [17] solution seems more dissipative. Moreover, the regions of high dissipation are concentrated at the satellite compartment end and at the booster region beginning. Temperatures close to 672.7 K are reached, less severe than the corresponding [17] temperature field.

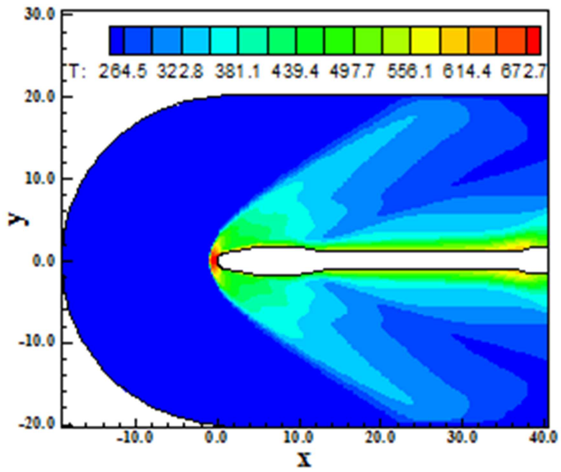

Figure 15. *Temperature contours (KK-C).*

As occurred with the Launder and Spalding option of the [16] turbulence model, no regions of circulation bubbles are captured by this model. The satellite compartment end and the booster region beginning are free of circulation bubble formation, which is a severe penalization to this turbulence model. This separation was captured by all turbulence models of this work and of [4; 24; 28], what becomes improbable its inexistence.

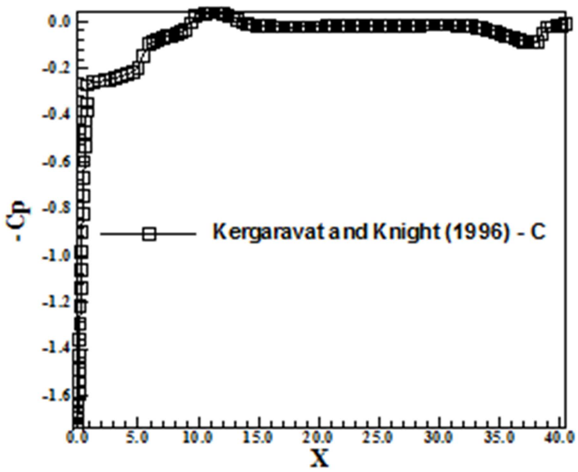

Figure 16. *–Cp distribution (KK-C).*

Figure 16 presents the –Cp distribution at wall of the VLS configuration, generated by the [16] turbulence model. This curve presents a reduction of –Cp close to the booster region and after that the pressure coefficient is recovered at the booster end. The –Cp distribution along the VLS central body is relative smooth, without oscillations in the solution. The –Cp distribution is in steps at the cockpit region.

5.3. Yoder, Georgiadids, and Orkwis Results

Figure 17 shows the pressure contours generated by the [2] scheme as using the [18] turbulence model. These contours are very similar to the contours of the [17] model. The shock is well captured and the solution is homogeneous, without pre-shock oscillations. The oblique shock at the ramp is also well captured by the turbulence model.

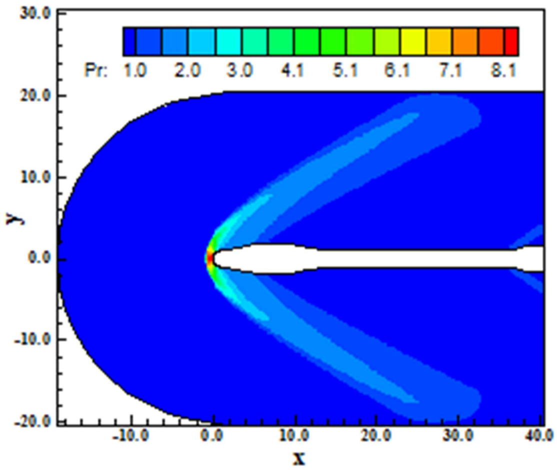

Figure 17. *Pressure contours (YGO).*

Figure 18 exhibits the Mach number contours obtained as using the [18] turbulence model. The solution is very close to the [16] solution, in both variants. It is possible to note that this solution presents less dissipation than the [17] solution. Regions of discrete formation of separation bubbles are perceptible at the downstream region of the satellite compartment and at the booster region. It is possible to be seen in Figs. 20 and 21 that circulation bubbles are well formed.

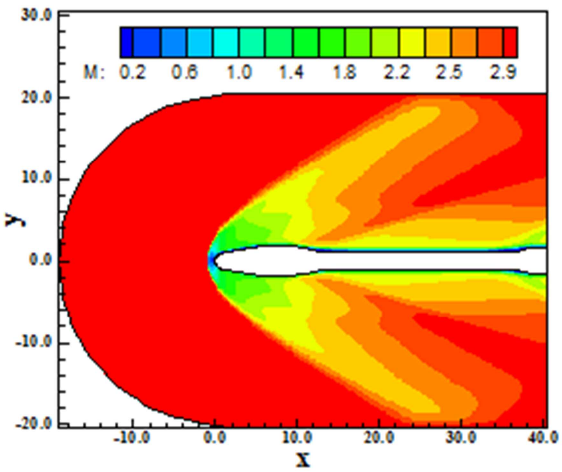

Figure 18. *Mach number contours (YGO).*

Figure 19 presents the translational temperature contours originated by the [2] scheme as using the [18] turbulence model. Temperatures near 837.8 K are observed in the field, superior to the respective fields in the [17] and [18] results.

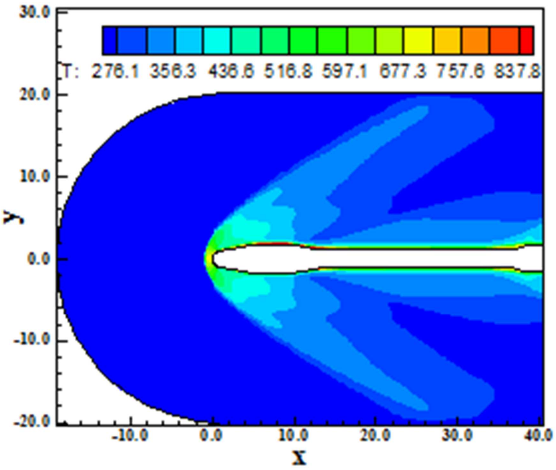

Figure 19. *Temperature contours (YGO).*

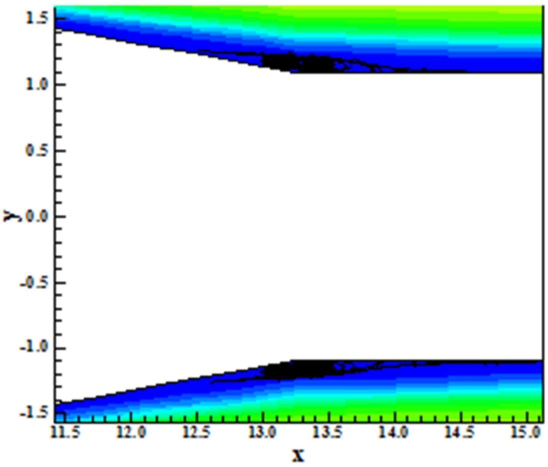

Figure 20. *Circulation bubble formation (Cockpit-YGO).*

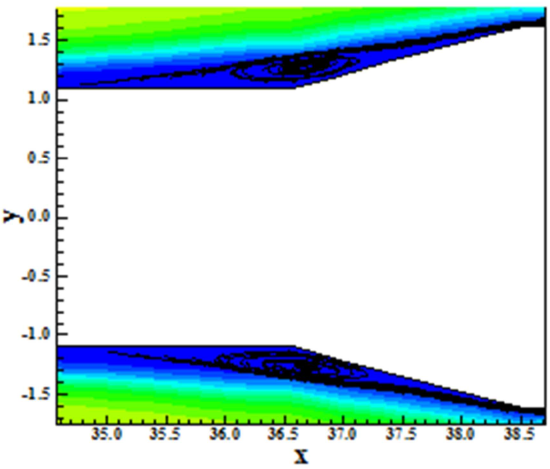

Figure 21. *Circulation bubble formation (Boosters-YGO).*

Figures 20 and 21 corroborate what was observed in the aforementioned paragraph. Circulation bubbles formation is originated at regions of high heating and generate loss of energy by the bubbles displacement and energy exchange due to collisions.

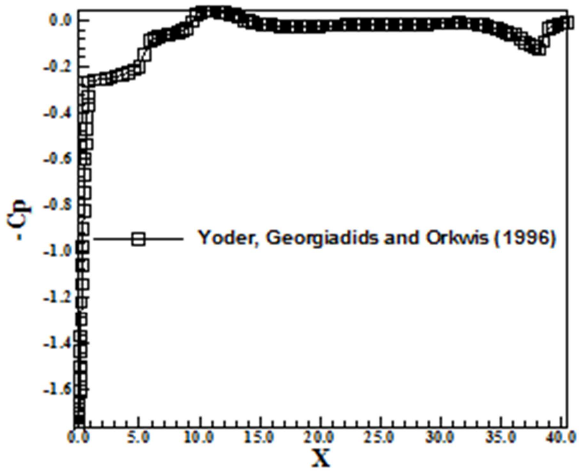

Figure 22. *–Cp distribution (YGO).*

Figure 22 exhibits the –Cp distribution originated by the [18] turbulence model. The cockpit upstream region presents a pressure distribution in steps and also presents the reduction of pressure close to the booster regions, with the subsequent increase of such pressure, obtained in all other solutions. The –Cp profile of the [18] turbulence model is similar to the –Cp profile of the [17] turbulence model.

5.4. Coakley Results

Figure 23 shows the pressure contours obtained by the [2] algorithm as the [19] turbulence model is employed. The curves of contours are well defined and the solution quality is the same as in the [17] solution. The shock at the booster region is well captured. No overshoots or undershoots are present, corroborating the idea of this scheme prevents Gibbs phenomenon.

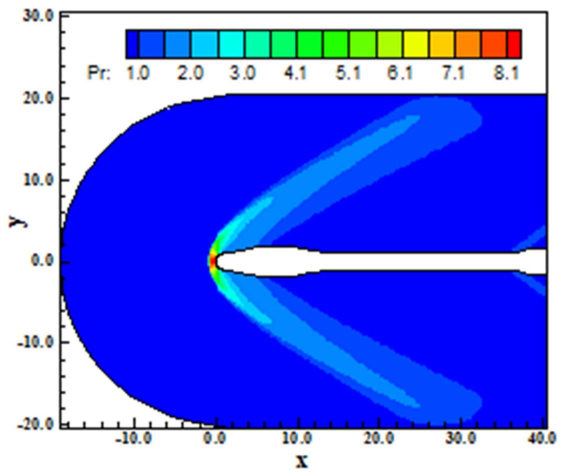

Figure 23. *Pressure contours (C).*

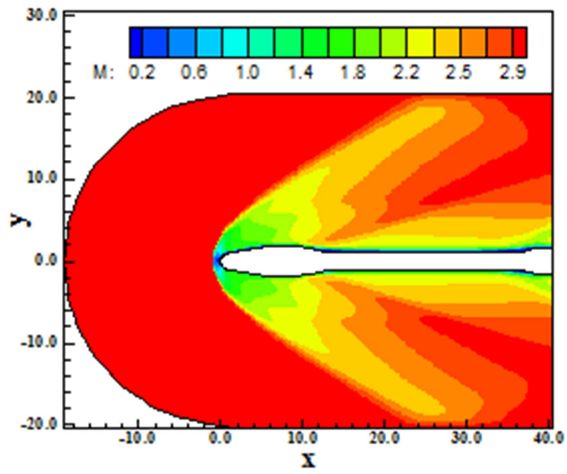

Figure 24. *Mach number contours (C).*

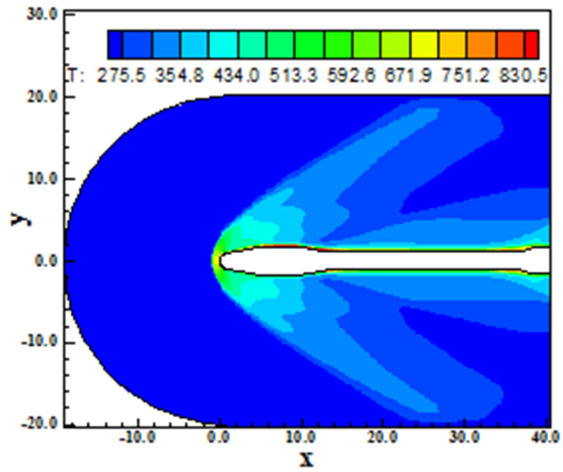

Figure 25. *Temperature contours (C).*

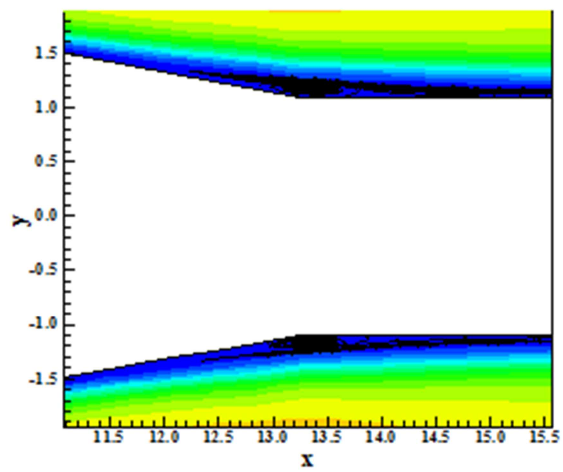

Figure 26. *Circulation bubble formation (Cockpit-C).*

Figure 24 exhibits the Mach number contours obtained by the [19] turbulence model. The contours present the same features of the [16, 17, 18] contours. No pre-shock oscillations are perceptible. The subsonic region is formed at the blunt nose as expected.

Figure 25 presents the translational temperature contours originated from the [19] turbulence model. The temperature peak is observed near to 830.5 K, which is less than the [18] temperature field. It is possible to detect regions of great heating near the satellite compartment end and at the booster regions. Corroborating this observation, circulation bubble formations were detected in these regions. Figures 26 and 27 show these regions. They are discrete, but observable, and ratifies the expected behavior.

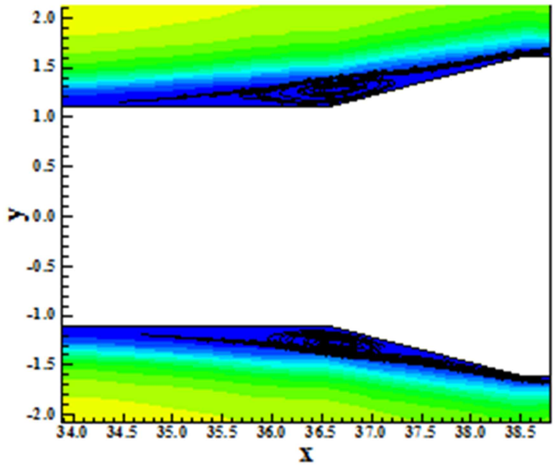

Figure 27. Circulation bubble formation (Boosters-C).

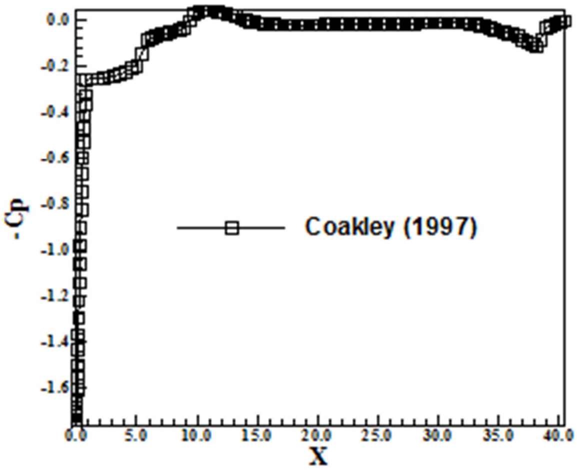

Figure 28. –Cp distribution (C).

Figure 28 shows the –Cp distribution obtained with the [19] turbulence model. The step profile at the blunt nose region and the hole region at the booster region are again observable. The pressure recovery at the booster region is typical of all solutions in this study. This –Cp profile is so strength than the [17] and [18] profiles.

5.5. Rumsey, Gatski, Ying, and Bertelrud Results

Figure 29 shows the pressure contours obtained by the [2] algorithm as the [20] turbulence model is employed. The curves of contours are well defined and the solution quality is the same as in the [17-19] solutions. The shock at the booster region is well captured. No overshoots or undershoots are present, corroborating the idea of this scheme prevents Gibbs phenomenon.

Figure 30 exhibits the Mach number contours obtained by the [20] turbulence model. The contours present the same features than the other corresponding contours. No pre-shock oscillations are perceptible. The subsonic region is formed at the blunt nose as expected.

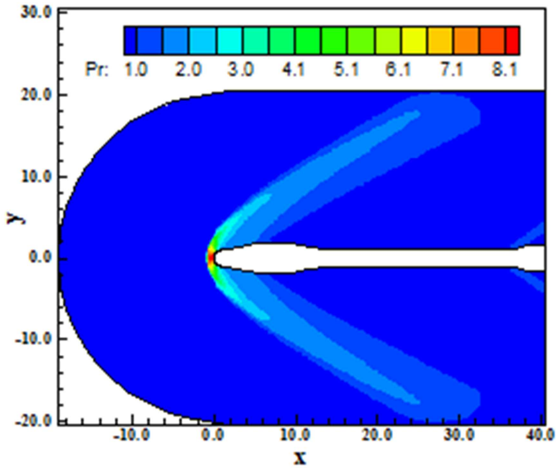

Figure 29. Pressure contours (RGYB).

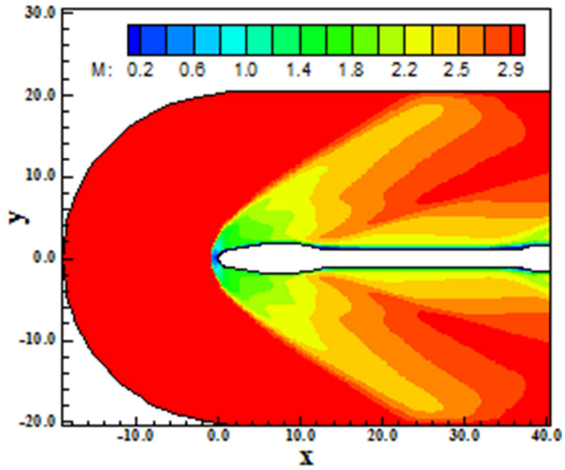

Figure 30. Mach number contours (RGYB).

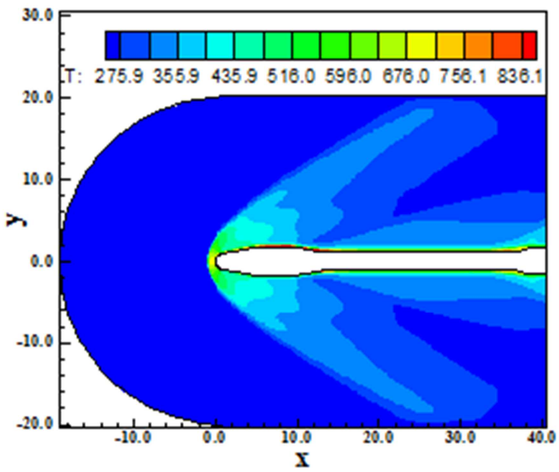

Figure 31. Temperature contours (RGYB).

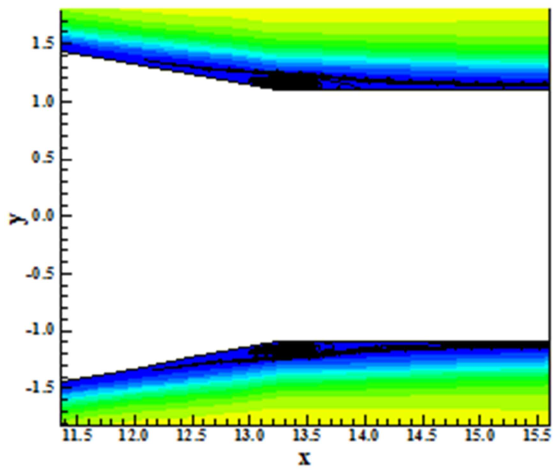

Figure 32. *Circulation bubble formation (Cockpit-RGYB).*

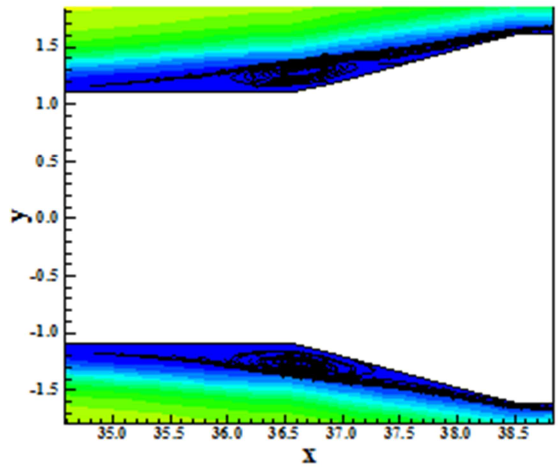

Figure 33. *Circulation bubble formation (Boosters-RGYB).*

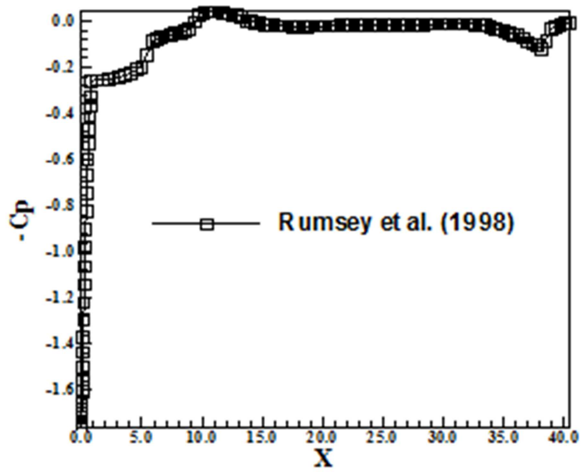

Figure 34. *–Cp distribution (RGYB).*

Figure 31 presents the translational temperature contours originated from the [20] turbulence model. The temperature peak is observed near to 836.1 K, which is less than the [18] temperature field and superior to the other fields. It is possible to detect regions of great heating near the satellite compartment end and at the booster regions. Confirming this observation, circulation bubble formations were detected in these regions. Figures 32 and 33 show these regions. They are discrete, but observable, and ratifies the expected behavior.

Figure 34 shows the –Cp distribution obtained with the [20] turbulence model. The step profile at the blunt nose region and the hole region at the booster region are again observable. The pressure recovery at the booster region is typical of all solutions in this study. This –Cp profile is so strength than the [17-19] profiles.

5.6. Quantitative Analysis

Table 3 shows the lift and drag aerodynamic coefficients calculated by the [2] scheme in the turbulent cases. As the geometry is symmetrical and an attack angle of zero value was adopted in the simulations, the lift coefficient should have a zero value. The most correct value to the lift coefficient is due to the [16] turbulence model, in its Launder and Spalding variant.

Table 3. *Aerodynamic coefficients of lift and drag.*

Turbulence Model:	c_L:	c_D:
[16] turbulence model – LS	-1.445×10^{-6}	0.072
[16] turbulence model – C	-4.390×10^{-6}	0.072
[17] turbulence model	-5.567×10^{-6}	0.073
[18] turbulence model	-8.085×10^{-6}	0.074
[19] turbulence model	4.887×10^{-6}	0.073
[20] turbulence model	-3.052×10^{-5}	0.074

Another possibility to quantitative comparison of the laminar and turbulent cases is the determination of the stagnation pressure ahead of the configuration. [25] presents a table of normal shock wave properties in its B Appendix. This table permits the determination of some shock wave properties as function of the freestream Mach number. In front of the VLS configuration, the shock wave presents a normal shock behavior, which permits the determination of the stagnation pressure, behind the shock wave, from the tables encountered in [25]. So it is possible to determine the ratio pr_0/pr_∞ from [25], where pr_0 is the stagnation pressure in front of the configuration and pr_∞ is the freestream pressure (equals to $1/\gamma$ to the present dimensionless).

Hence, to this problem, $M_\infty = 3.0$ corresponds to $pr_0/pr_\infty = 12.06$ and remembering that $pr_\infty = 0.714$, it is possible to conclude that $pr_0 = 8.61$. Values of the stagnation pressure to the turbulent cases and respective percentage errors are shown in Tab. 4. They are obtained from Figures 3, 9, 13, 17, 23 and 29. As can be observed, with the exception of the [17] turbulence model, all others presented the best result, with a percentage error of 5.80%.

Table 4. *Values of the stagnation pressure and respective percentage errors.*

Turbulence Model:	pr_0:	Error (%):
[16] turbulence model – LS	8.10	5.80
[16] turbulence model – C	8.10	5.80
[17] turbulence model	8.00	7.00
[18] turbulence model	8.10	5.80
[19] turbulence model	8.10	5.80
[20] turbulence model	8.10	5.80

Finally, Table 5 exhibits the computational data of the present simulations. It can be noted that the most efficient is the [18] turbulence model.

Table 5. *Computational data.*

Turbulence Model:	CFL:	Iterations:
[16] turbulence model – LS	0.05	11,415
[16] turbulence model – C	0.05	12,950
[17] turbulence model	0.10	6,050
[18] turbulence model	0.10	4,315
[19] turbulence model	0.10	5,220
[20] turbulence model	0.10	4,735

As final conclusion of this study, the [16] turbulence model in its Launder and Spalding variant was the best when comparing these five turbulence models: [16-20]. This choice is based on the best estimative of the aerodynamic coefficients and the best estimative to the stagnation pressure.

6. Conclusion

In the present work, the [2] flux vector splitting scheme is implemented, on a finite-volume context. The two-dimensional Favre-averaged Navier-Stokes equations are solved using an upwind discretization on a structured mesh. The [16-20] two-equation models are used in order to close the problem. The physical problem under study is the supersonic flow around a simplified version of the VLS configuration. The implemented scheme uses a MUSCL procedure to reach second order accuracy in space. The time integration uses a Runge-Kutta method of five stages and is second order accurate. The algorithm is accelerated to the steady state solution using a spatially variable time step. This technique has proved excellent gains as reported in [21-22].

The results have demonstrated that the [16] model in its Launder and Spalding variant has yielded more critical pressure field than the other models. The aerodynamic coefficient of lift is better predicted by the [16] turbulence model in its Launder and Spalding variant. Finally, the stagnation pressure ahead of the VLS configuration is better predicted by the [16] turbulence model in its Launder and Spalding variant. Hence, the best choice corresponds to the [16] turbulence model in its LS variant for this study.

Finally, the last paper of this work will treat the [6], [30], [31] and [16] turbulence models applied to an aerospace problem aiming determine the best turbulence model among these ones.

Acknowledgment

The author would like to thank the infrastructure of ITA that allowed the realization of this work.

References

[1] P. Kutler, “Computation of Three-Dimensional, Inviscid Supersonic Flows”, *Lecture Notes in Physics*, vol. 41, pp. 287-374, 1975.

[2] B. Van Leer, “Flux-Vector Splitting for the Euler Equations”, Proceedings of the 8th International Conference on Numerical Methods in Fluid Dynamics, E. Krause, Editor, *Lecture Notes in Physics*, vol. 170, pp. 507-512, Springer-Verlag, Berlin, 1982.

[3] R. Radespiel, and N. Kroll, “Accurate Flux Vector Splitting for Shocks and Shear Layers”, *Journal of Computational Physics*, vol. 121, pp. 66-78, 1995.

[4] E. S. G. Maciel, “Assessment of Several Turbulence Models as Applied to Supersonic Flows in 2D – Part I”, *Engineering and Technology*, Vol. 2, Issue 4, 2015, June, pp. 220-234.

[5] E. S. G. Maciel, and N. G. C. R. Fico Jr., “Estudos de Escoamentos Turbulentos Utilizando o Modelo de Baldwin e Lomax e Comparação entre Algoritmos Explícitos e Implícitos”, *Proceedings of the III National Congress of Mechanical Engineering (III CONEM)*, Belém, PA, Brazil, 2004. [CD-ROM]

[6] B. S. Baldwin, and H. Lomax, “Thin Layer Approximation and Algebraic Model for Separated Turbulent Flows”, *AIAA Paper 78-257*, 1978.

[7] R. W. MacCormack, “The Effect of Viscosity in Hypervelocity Impact Cratering”, *AIAA Paper 69-354*, 1969.

[8] T. H. Pulliam, and D. S. Chaussee, “A Diagonal Form of an Implicit Approximate-Factorization Algorithm”, *Journal of Computational Physics*, vol. 39, pp. 347-363, 1981.

[9] A. Jameson, W. Schmidt, and E. Turkel, “Numerical Solution of the Euler Equations by Finite Volume Methods Using Runge-Kutta Time Stepping Schemes”, *AIAA Paper 81-1259*, 1981.

[10] E. S. G. Maciel, and N. G. C. R. Fico Jr., “High Resolution Algorithms Coupled with Three Turbulence Models Applied to an Aerospace Flow Problem – Part I”, *AIAA Paper 06-0292*, 2006. [CD-ROM]

[11] T. Cebeci, and A. M. O. Smith, “A Finite-Difference Method for Calculating Compressible Laminar and Turbulent Boundary Layers”, *Journal of Basic Engineering,* Trans. ASME, Series B, vol. 92, no. 3, pp. 523-535, 1970.

[12] P. R. Sparlat, and S. R. Allmaras, “A One-Equation Turbulence Model for Aerodynamic Flows”, *AIAA Paper 92-0439*, 1992.

[13] A. Harten, “High Resolution Schemes for Hyperbolic Conservation Laws”, *Journal of Computational Physics*, vol. 49, pp. 357-393, 1983.

[14] E. S. G. Maciel, and N. G. C. R. Fico Jr., “Comparação Entre Modelos de Turbulência de Duas Equações Aplicados a um Problema Aeroespacial”, *Proceedings of the Primer Congreso Argentino de Ingeniería Mecánica (I CAIM),* Bahía Blanca, Argentina, 2008. [CD-ROM]

[15] F. Jacon, and D. Knight, “A Navier-Stokes Algorithm for Turbulent Flows Using an Unstructured Grid and Flux Difference Splitting”, *AIAA Paper 94-2292*, 1994.

[16] Y. Kergaravat, and D. Knight, “A Fully Implicit Navier-Stokes Algorithm for Unstructured Grids Incorporating a Two-Equation Turbulence Model”, *AIAA Paper 96-0414*, 1996.

[17] G. Zhou, L. Davidson, and E. Olsson, “Turbulent Transonic Airfoil Flow Simulation Using a Pressure-Based Algorithm”, *AIAA Journal*, Vol. 33, No. 1, January, pp. 42-47, 1995.

[18] D. A. Yoder, N. J. Georgiadids, and P. D. Orkwis, 1996, "Implementation of a Two-Equation K-Omega Turbulence Model in NPARC", *AIAA Paper 96-0383*.

[19] T. J. Coakley, "Development of Turbulence Models for Aerodynamic Applications", *AIAA Paper 97-2009*, 1997.

[20] C. L. Rumsey, T. B. Gatski, S. X. Ying, and A. Bertelrud, "Prediction of High-Lift Flows Using Turbulent Closure Models", *AIAA Journal*, Vol. 36, No. 5, May, pp. 765-774, 1998.

[21] E. S. G. Maciel, "Analysis of Convergence Acceleration Techniques Used in Unstructured Algorithms in the Solution of Aeronautical Problems – Part I", *Proceedings of the XVIII International Congress of Mechanical Engineering (XVIII COBEM)*, Ouro Preto, MG, Brazil, 2005. [CD-ROM]

[22] E. S. G. Maciel, "Analysis of Convergence Acceleration Techniques Used in Unstructured Algorithms in the Solution of Aerospace Problems – Part II", *Proceedings of the XII Brazilian Congress of Thermal Engineering and Sciences (XII ENCIT)*, Belo Horizonte, MG, Brazil, 2008. [CD-ROM]

[23] R. W. Fox, and A. T. McDonald, "*Introdução à Mecânica dos Fluidos*", Ed. Guanabara Koogan, Rio de Janeiro, RJ, Brazil, 632 p, 1988.

[24] E. S. G. Maciel, "Assessment of Several Turbulence Models as Applied to Supersonic Flows in 2D – Part II", Submitted to *Engineering and Technology* (under review), 2015.

[25] J. D. Anderson Jr., "*Fundamentals of Aerodynamics*", McGraw-Hill, Inc., EUA, 563p, 1984.

[26] K. Y. Chien, "Predictions of Channel and Boundary Layer Flows with a Low-Reynolds-Number Turbulence Model", *AIAA Journal*, Vol. 20, January, pp. 33-38, 1982.

[27] C. G. Speziale, S. Sarkar, and T. B. Gatski, "Modeling the Pressure-Strain Correlation of Turbulence: An Invariant Dynamical Systems Approach", Journal of Fluid Mechanics, Vol. 227, pp. 245-272, 1991.

[28] E. S. G. Maciel, "Assessment of Several Turbulence Models as Applied to Supersonic Flows in 2D – Part III", *Engineering and Technology*, Vol. 2, Issue 4, 2015, June, pp. 235-255.

[29] B. E. Launder, and D. B. Spalding, "The Numerical Computation of Turbulent Flows", *Computer Methods in Applied Mechanics and Engineering*, vol. 3, pp. 269-289, 1974.

[30] D. C. Wilcox, "Reassessment of the Scale-Determining Equation for Advanced Turbulence Models", *AIAA Journal*, Vol. 26, November, pp. 1299-1310, 1988.

[31] F. R. Menter, and C. L. Rumsey, "Assessment of Two-Equation Turbulence Models for Transonic Flows", *AIAA Paper 94-2343*, 1994.